Supercooled liquid water clouds observed over Dome C, Antarctica: temperature sensitivity and cloud radiative forcing

Philippe Ricaud[1], Massimo Del Guasta[2], Angelo Lupi[3], Romain Roehrig[1], Eric Bazile[1], Pierre Durand[4], Jean-Luc Attié[4], Alessia Nicosia[3] and Paolo Grigioni[5]

[1]CNRM, Université de Toulouse, Météo-France, CNRS, Toulouse, France (philippe.ricaud@meteo.fr; romain.roehrig@meteo.fr; eric.bazile@meteo.fr)

[2]INO-CNR, Sesto Fiorentino, Italy (massimo.delguasta@ino.cnr.it)

[3]ISAC-CNR, Bologna, Italy (a.lupi@isac.cnr.it; a.nicosia@isac.cnr.it)

[4]Laboratoire d'Aérologie, Université de Toulouse, CNRS, UPS, Toulouse, France (pierre.durand@aero.obs-mip.fr; jean-luc.attie@aero.obs-mip.fr)

[5]ENEA, Roma, Italy (paolo.grigioni@enea.it)

Correspondence: philippe.ricaud@meteo.fr

27 November 2023, Version REV03 V02

Submitted to **Atmospheric Chemistry and Physics**

Abstract

Clouds affect the Earth climate with an impact that depends on the cloud nature (solid/ liquid water). Although the Antarctic climate is changing rapidly, cloud observations are sparse over Antarctica due to few ground stations and satellite observations. The Concordia station is located on the East Antarctic Plateau (75°S, 123°E, 3233 m above mean sea level), one of the driest and coldest places on Earth. We used observations of clouds, temperature, liquid water and surface irradiance performed at Concordia during 4 austral summers (December 2018-2021) to analyse the link between liquid water and temperature and its impact on surface irradiance in the presence of supercooled liquid water (liquid water for temperature less than 0°C) clouds (SLWCs). Our analysis shows that, within SLWCs, temperature logarithmically increases from -36.0°C to -16.0°C when liquid water path increases from 1.0 to 14.0 g m^{-2}. The SLWC radiative forcing is positive and logarithmically increases from 0.0 to 70.0 W m^{-2} when liquid water path increases from 1.2 to 3.5 g m^{-2}. This is mainly due to the downward longwave component that logarithmically increases from 0 to 90 W m^{-2} when liquid water path increases from 1.0 to 3.5 g m^{-2}. The attenuation of shortwave incoming irradiance (that can reach more than 100 W m^{-2}) is almost compensated for by the upward shortwave irradiance because of high values of surface albedo. Based on our study, we can extrapolate that, over the Antarctic continent, SLWCs have a maximum radiative forcing rather weak over the Eastern Antarctic Plateau (0 to 7 W m^{-2}) but 3 to 5 times larger over Western Antarctica (0 to 40 W m^{-2}), maximizing in summer and over the Antarctic Peninsula.

1. Introduction

Antarctic clouds play an important role in the climate system by influencing the Earth's radiation balance, both directly at high southern latitudes and, indirectly, at the global level through complex teleconnections (Lubin et al., 1998). However, in Antarctica, ground stations are mainly located on the coast and yearlong observations of clouds and associated meteorological parameters are scarce. Meteorological analyses and satellite observations of clouds can nevertheless give some information on cloud properties suggesting that clouds vary geographically, with a fractional cloud cover ranging from about 50 to 60% around the South Pole to 80-90% near the coast (Bromwich et al., 2012; Listowski et al., 2019). In situ aircraft measurements performed mainly over the Western Antarctic Peninsula (Grosvenor et al., 2012; Lachlan-Cope et al., 2016) and nearby coastal areas (O'Shea et al., 2017) provided new insights to polar cloud modelling and highlighted sea-ice production of Cloud-Condensation Nuclei (CCN) and Ice Nucleating Particles (INPs) (see e.g. Legrand et al., 2016). Mixed-phase clouds (made of solid and liquid water) are preferably observed near the coast (Listowski et al., 2019) with larger ice crystals and water droplets (Lachlan-Cope, 2010; Lachlan-Cope et al., 2016; Grosvenor et al., 2012; O'Shea et al., 2017; Grazioli et al., 2017). Based on the raDAR/liDAR-MASK (DARDAR) spaceborne products (Listowski et al., 2019), it has been found that clouds are mainly constituted of ice above the continent. The abundance of Supercooled Liquid Water (SLW, the water staying in liquid phase below 0°C) clouds depends on temperature and liquid/ice fraction. It decreases sharply poleward, and is two to three times lower over the Eastern Antarctic Plateau than over the Western Antarctic. Furthermore, the nature and optical properties of the clouds depend on the type and concentration of CCN and INPs. Bromwich et al. (2012) mention in their review paper that CCN and INPs are of various nature and large uncertainties exist relative to their origin and abundance over Antarctica. An important point remains the inability of both research and operational weather prediction models to accurately

represent the clouds (especially SLW clouds, SLWCs) in Antarctica causing biases of several tens W m^{-2} on net surface irradiance (Listowski and Lachlan-Cope, 2017; King et al., 2006, 2015; Bromwich et al., 2013) over and beyond the Antarctic (Lawson and Gettelman, 2014; Young et al. 2019). From year-long LIDAR observations of mixed-phase clouds at South Pole (Lawson and Gettelman, 2014), SLWCs were shown to occur more frequently than in earlier aircraft observations or weather model simulations, leading to biases in the surface radiation budget estimates.

Liquid water in clouds may occur in supercooled form due to a relative lack of ice nuclei for temperature greater than -39°C and less than 0°C. Very little SLW is then expected because the ice crystals that form in this temperature range will grow at the expense of liquid droplets (called the "Wegener-Bergeron-Findeisen" process; Wegener, 1911; Bergeron, 1928; Findeisen, 1938; Storelvmo and Tan, 2015). Nevertheless, SLW is often observed at negative temperatures higher than -20°C at all latitudes being a danger to aircraft since icing on the wings and airframe can occur, reducing lift, and increasing drag and weight. As temperature decreases to -36°C, SLW dramatically lessens, so it is highly difficult 1) to observe SLWCs and 2) to quantify the amount of liquid water present in SLWCs. But during the Year Of Polar Prediction (YOPP) international campaign, recent observations performed at the Dome C station in Antarctica of two case studies in December 2018 have revealed SLWCs with temperature between -20°C and -30°C and Liquid Water Path (LWP, the liquid water content integrated along the vertical) between 2 to 20 g m^{-2}, as well as a considerable impact on the net surface irradiance that exceeded the simulated values by 20 to 50 W m^{-2} (Ricaud et al., 2020).

The Dome C (Concordia) station, jointly operated by French and Italian institutions in the Eastern Antarctic Plateau (75°06'S, 123°21'E, 3233 m above mean sea level, amsl), is one of the driest and coldest places on Earth with surface temperatures ranging from about -20°C in summer to -70°C in winter. There are four main instruments relevant to this study that have

been routinely running for about 10 years: 1) The H_2O Antarctica Microwave Stratospheric and Tropospheric Radiometer (HAMSTRAD, Ricaud et al., 2010a) to obtain vertical profiles of temperature and water vapour, as well as the LWP. 2) The tropospheric depolarization LIDAR (Tomasi et al., 2015) to obtain vertical profiles of backscatter and depolarization to be used for the detection of SLWCs. 3) An Automated Weather Station (AWS) to provide screen-level air temperature. And 4) the Baseline Surface Radiation Network (BSRN) station to measure downward and upward longwave (4 to 50 μm) and shortwave (0.3 to 3 μm) surface irradiances (F) from which the net surface irradiance (F_{Net}), calculated as the difference between the downward and upward components, can be computed (Driemel et al., 2018) as:

$$F_{Net} = \left(F_{LW}^{Down} - F_{LW}^{Up}\right) + \left(F_{SW}^{Down} - F_{SW}^{Up}\right) \quad (1)$$

where F_{LW}^{Down}, F_{LW}^{Up}, F_{SW}^{Down}, and F_{SW}^{Up} represent the downward longwave, upward longwave, downward shortwave and upward shortwave surface irradiances, respectively.

At a given time, the impact of a cloud on the surface irradiance is estimated from the difference between the net irradiance, in cloudy ($F_{Net,cld}$) and cloud-free (FCF_{Net}) conditions to provide the so-called "cloud radiative forcing" ΔF_{Net} (e.g., Stapf et al., 2020):

$$\Delta F_{Net} = F_{Net,cld} - FCF_{Net} \quad (2)$$

A similar equation can be written for each of the four irradiances that appear in the right-hand side of equation (1). The aim of the present study is double. Using observations performed at Concordia, we intend to quantify the link between 1) temperature in the SLWCs and LWP and 2) SLWC radiative forcing and LWP.

The article is structured as follows. Section 2 presents the instruments during the period of study. In section 3, we detail the methodology employed to detect the SLWCs and calculate their cloud radiative forcing, and we present the statistical method to emphasize the relationship between in-cloud temperature and LWP on the one hand, and cloud radiative forcing and LWP

on the other hand. The results are highlighted in section 4 and discussed in section 5, before concluding in section 6.

2. Instruments

We have used the observations from 4 instruments held at the Dome C station, namely the LIDAR instrument to classify the cloud as SLWC, the HAMSTRAD microwave radiometer to obtain LWP and vertical profile of temperature, the AWS to obtain screen-level air temperature and the BSRN network to measure the surface irradiances (F_{LW}^{Down}, F_{LW}^{Up}, F_{SW}^{Down}, and F_{SW}^{Up}) to obtain F_{Net}.

2.1. LIDAR

The tropospheric depolarization LIDAR (532 nm) has been operating at Dome C since 2008 (see http://lidarmax.altervista.org/englidar/_Antarctic%20LIDAR.php). The LIDAR provides 5-min tropospheric profiles of clouds characteristics continuously, from 20 to 7000 m above ground level (agl), with a resolution of 7.5 m. For the present study, the most relevant parameter is the LIDAR depolarization ratio (Mishchenko et al., 2000) that is a robust indicator of non-spherical shape for randomly oriented cloud particles. A depolarization ratio below 10% is characteristic of SLWC, while higher values are produced by ice particles. The possible ambiguity between SLW droplets and oriented ice plates is avoided at Dome C by operating the LIDAR 4° off-zenith (Hogan and Illingworth, 2003).

2.2. HAMSTRAD

HAMSTRAD is a microwave radiometer that profiles water vapour, liquid water and tropospheric temperature above Dome C. Measuring at both 60 GHz (oxygen molecule line (O_2) to deduce the temperature) and 183 GHz (H_2O line), this unique, state-of-the-art radiometer was installed on site for the first time in January 2009 (Ricaud et al., 2010a and b). The measurements of the HAMSTRAD radiometer allow the retrieval of the vertical profiles

of water vapour and temperature from the ground to 10-km altitude with vertical resolutions of 30 to 50 m in the Planetary Boundary Layer (PBL), 100 m in the lower free troposphere and 500 m in the upper troposphere-lower stratosphere. The integral along the vertical of the water vapour concentration gives the integrated water vapour (IWV). The time resolution is adjustable and fixed at 60 seconds since 2018. Note that an automated internal calibration is performed every 12 atmospheric observations and lasts about 4 minutes. Consequently, the atmospheric time sampling is 60 seconds for a sequence of 12 profiles and a new sequence starts 4 minutes after the end of the previous one. The temporal resolution on the instrument allows for detection and analysis of atmospheric processes such as the diurnal evolution of the PBL (Ricaud et al., 2012) and the presence of clouds and diamond dust (Ricaud et al., 2017) together with SLWCs (Ricaud et al., 2020). In addition, the LWP (g m^{-2}) that gives the amount of liquid water integrated along the vertical can also be estimated. Observations of LWP have been performed when the instrument was installed at the Pic du Midi station (2877 amsl, France) during the calibration/validation period in 2008 prior to its set up in Antarctica in 2009 (Ricaud et al., 2010a) and during the Year Of Polar Prediction (YOPP) campaign in summer 2018-2019 (Ricaud et al., 2020). At the present time, it has not yet been possible to compare HAMSTRAD LWP retrievals with observations from other instruments, neither at the Pic du Midi nor at Dome C stations. To better evaluate its performance, the 2021-2022 and the future 2022-2023 summer campaigns are dedicated to in-situ observations of SLWCs. Comparisons with numerical weather prediction models were showing consistent amounts of LWP at Dome C when the partition function between ice and liquid water was favouring SLW for temperatures less than 0°C (Ricaud et al., 2020). Note that microwave observations at 60 and 183 GHz are not sensitive to ice crystals. This has already been discussed in Ricaud et al. (2017) when considering the study of diamond dust in Antarctica. As a consequence, possible precipitation

of ice, within or below SLW clouds, as detected by the LIDAR, does not affect the retrievals of temperature, water vapour and liquid water.

2.3. AWS

An American Automated Weather Station (AWS) is installed at Concordia about 500 m away from the station and can provide screen-level air temperature (T_a) every 10 minutes. Data are freely available at https://amrc.ssec.wisc.edu/data/archiveaws.html.

2.4. BSRN

The BSRN sensors at Dome C are mounted at the Astroconcordia/Albedo-Rack sites, with upward and downward looking, heated and ventilated Kipp&Zonen CM22 pyranometers and CG4 pyrgeometers providing measurements of hemispheric downward and upward broadband shortwave (SW, 0.3 to 3 μm) and longwave (LW, 4 to 50 μm) horizontal irradiances at the surface, respectively. These data are used to retrieve values of net surface irradiances. All these measurements follow the rules of acquisition, quality check and quality control of the BSRN (Driemel et al., 2018).

2.5. Period of study

From the climatological study presented in Ricaud et al. (2020), the SLWCs are mainly observed above Dome C in summer, with a higher occurrence in December than in January: 26% in December against 19% in January representing the percentage of days per month that SLW clouds were detected during the YOPP campaign (summer 2018-2019) within the LIDAR data for more than 12 hours per day. We have thus concentrated our analysis on December and the 4 years: 2018-2021. Since we have to use the four data sets (LIDAR, HAMSTRAD, AWS and BSRN) in time coincidence, the actual number of days per year and the time sampling for each day selected in our analysis are detailed in Table 1.

3. Methodology

3.1. SLWC detection

Consistent with Ricaud et al. (2020), we use LIDAR observations to discriminate between SLW and ice in a cloud. High values of LIDAR backscatter coefficient ($\beta > 100\ \beta_{mol}$, with β_{mol} the molecular backscatter) associated with very low depolarization ratio (<5%) signifies the presence of an SLWC whilst high depolarization ratio (>20%) indicates the presence of an ice cloud or precipitation. Once the SLWC is detected both in time and altitude, the temperature (T) profile within the cloud and the LWP measured by the HAMSTRAD radiometer in time coincidence are selected together with the surface irradiances observed by the BSRN instruments.

The LIDAR profiles are interpolated along the temperature vertical grid and then according to the temperature time sampling. As a consequence, for a given time and height, we have a depolarization ratio, a backscatter value, a temperature as well as (not height-dependent) IWV and LWP values. BSRN irradiances are time interpolated to be coincident with the other parameters. So, for a given time, we have a set of BSRN irradiances (F_{LW}^{Down}, F_{LW}^{Up}, F_{SW}^{Down}, F_{SW}^{Up} and F_{Net}) and an LWP. At a (time, height) point showing high backscatter signal and low depolarization, the associated parameters (temperature, LWP and irradiances) are flagged as "SLW cloud". The statistic is thus done using all the SLW-flagged points without any averaging. The temperature corresponds to the in-cloud temperature.

Figure 1 shows, as a typical example, the time evolution of the LIDAR backscatter coefficient and depolarization ratio, as well as the HAMSTRAD LWP and temperature vertical profile for the 27 December 2021. Associated with the SLWCs, the LWP values are between 1.0 and 3.0 g m^{-2}. The SLWCs are present over a temperature range varying from about -28.0 °C to -33.0 °C. Note the cloud present at 04:00-05:00 UTC that is not labelled as a SLWC but rather as an ice cloud (high backscatter and high depolarization signals) with no associated increase of LWP and temperature above -28.0 °C.

Figure 2 highlights the time evolution of the SLWC obtained on 27 December 2021 together with some snapshots from the HALO-CAM video camera taken with or without SLWC on: 01:00 (no SLWC), 07:19 (SLWC), 09:00 (no SLWC), 10:14 (SLWC), 13:00 (no SLWC), 16:03 (SLWC), 18:01 (no SLWC) and 20:53 UTC (SLWC). SLWCs (high backscatter and low depolarization signals) are clearly detected at 07:00-08:00, 10:00-11:00, 16:00-17:00, 21:00-22:00 and 23:00-24:00 UTC over an altitude range 500 to 1000 m above ground level (agl). In general, SLWCs observed over the station did not correspond to overcast conditions.

3.2. Cloud Radiative Forcing

From equation (2), one of the main difficulties in computing the cloud radiative forcing (ΔF_{Net}) is to estimate FCF_{Net} from its individual components, namely the cloud-free downward longwave, upward longwave, downward shortwave and upward shortwave surface irradiances. We performed several studies (reference irradiances measured over days when clouds are absent, radiative transfer calculations) from which it resulted that the most robust method was to use a parameterization of the cloud-free downward longwave and shortwave surface irradiances widely used in the community. In Dutton et al. (2004), cloud-free downward shortwave surface irradiance (FCF_{SW}^{Down}) is parameterized as:

$$FCF_{SW}^{Down} = a\ \cos(z)^b\ c^{\left(\frac{1}{\cos(z)}\right)} \quad (3)$$

where z is the solar-zenith angle, and a, b, and c are coefficients optimized using well-identified cloud-free situations. In Dupont et al. (2008), cloud-free downward longwave surface irradiance (FCF_{LW}^{Down}) is parameterized as:

$$FCF_{LW}^{Down} = \varepsilon_a\ \sigma\ T_a^4 \quad (4)$$

where T_a is the screen-level air temperature in Kelvin (K), σ the Stephan-Boltzmann's constant and ε_a the apparent atmospheric emissivity. The latter is supposed to be a function of the integrated water vapor (IWV) following the equation:

$$\varepsilon_a = 1 - (1 + IWV)\exp(-(d + e \times IWV)^f) \quad (5)$$

where *d*, *e* and *f* are coefficients that need to be optimized using cloud-free situations and IWV is provided by the HAMSTRAD measurements. The cloud-free upward shortwave surface irradiance (FCF_{SW}^{Up}) is evaluated from FCF_{SW}^{Down} with the surface albedo ($A_{BSRN} = F_{SW}^{Up}(BSRN)/F_{SW}^{Down}(BSRN)$) calculated from observations:

$$FCF_{SW}^{Up} = A_{BSRN} \times FCF_{SW}^{Down} \quad (6)$$

where $F_{SW}^{Up}(BSRN)$ and $F_{SW}^{Down}(BSRN)$ are the upward and downward shortwave surface irradiance measured by the BSRN instruments, respectively. With this method, we take into account the actual shape of the surface, and in particular its rough structure caused by the sastrugi (see section 5.5). Thus, the surface albedo varies with the sun angles (azimutal and zenithal) and cannot be considered as constant over the diurnal cycle.

The cloud-free upward longwave radiation (FCF_{LW}^{Up}) is evaluated as:

$$FCF_{LW}^{Up} = \varepsilon_s \, \sigma T_s^4 + (1 - \varepsilon_s) \, FCF_{LW}^{Down} \quad (7)$$

where T_s is the surface temperature and the surface emissivity ε_s is assumed constant and equal to 0.99. T_s is diagnosed based on equation (7) by using the BRSN upward and downward longwave surface irradiances.

Cloud-free situations are detected based on visual inspection of the LIDAR (depolarization) measurements. Depolarization ratios greater than about 1% are attributed to the presence of cloud (cirrus, mixed-phase, SLW), diamond dust, fog, etc. Thus, within each 24-hour slot covering the Decembers 2018-2021, the 1-hour periods when the depolarization ratios are less than 1% are considered as cloud-free periods. Consequently, to evaluate the surface cloud-free irradiances over the month of December and the years 2018-2021, we need to have coincident observations from the 4 BSRN instruments, the LIDAR (depolarization), HAMSTRAD and the AWS (see Table 1).

Once cloud-free situations are identified, the parametric coefficients *a-f* are estimated minimizing a least-square cost function using the trust region reflective method (e.g., Branch

et al., 1999). To assess the robustness of the estimated coefficient values, a K-fold cross-validation is performed. The learning dataset is split into 10 subsamples of equal size. Nine of them are selected to optimize the coefficient and the validation is conducted on the remaining subsample. The exercise is performed 10 times. The results are summarized below. Note that following Dupont et al. (2008), f is assumed to be equal to 1.0, and therefore not optimized.

For cloud-free downward shortwave surface irradiance, the K-fold cross-validation provides the following K-fold average value (K-fold minimum and maximum are indicated within brackets): a = 1360.7 [1360.5, 1360.8] W m^{-2}; b = 0.990 [0.989, 0.991]; c = 0.964 [0.964, 0.965] giving a bias of -0.002 [-0.317, 0.251] W m^{-2} and a RMSE of 14.9 [10.8, 16.5] W m^{-2}. Similarly, for cloud-free downward longwave surface irradiance, the K-fold cross-validation provides the following results: d = 0.723 [0.722, 0.724]; e = 3.58 [3.57, 3.59] kg^{-1} m^2; f = 1.0 giving a bias of 0.34 [-0.005, 0.87] W m^{-2} and a RMSE of 9.26 [8.92, 9.58] W m^{-2}. These coefficient values are then used to compute cloud-free surface irradiances at a 1-min time resolution.

Figure 3 shows the time evolution of the cloud radiative forcing (ΔF_{net}) and the individual components (ΔF_{LW}^{Down}, ΔF_{LW}^{Up}, ΔF_{SW}^{Down} and ΔF_{SW}^{Up}) calculated for 27 December 2021 when SLWCs are present (see Figures 1 and 2). Associated with the SLWCs, on the one hand, ΔF_{LW}^{Down} increases to values of 40 to 90 W m^{-2}, whilst the impact on ΔF_{LW}^{Up} is negligible (±2 W m^{-2}). On the other hand, ΔF_{SW}^{Down} and ΔF_{SW}^{Up} both similarly decrease by 80 to 150 W m^{-2}. The effect on ΔF_{net} is obviously positive (0 to 80 W m^{-2}) with some weak negative values (from 0 to -10 W m^{-2}) when SWLCs just appear or disappear that can possibly come from the inhomogeneity of the cloud distribution. Spikes can be attributed to cloud edge effects, when a fraction of the direct shortwave incident radiation and an additional diffuse contribution scattered from cloud edges fall on the radiation sensor.

We now want to statistically analyse all the ΔF calculated in December 2018-2021 in order to assess the SLWC radiative forcing as a function of LWP and to investigate the sensitivity of the temperature inside the SLWCs as a function of LWP.

3.3. Statistical Method

The datasets corresponding to SLWCs periods are binned into 1°C-wide bins for in-cloud temperature T, 0.2 g m^{-2}-wide bins for LWP, and 5 W m^{-2}-wide bins for ΔF. The number of points per bin is calculated for all the paired datasets, namely T-LWP, and ΔF-LWP (ΔF_{net}-LWP, ΔF_{LW}^{Down}-LWP, ΔF_{LW}^{Up}-LWP, ΔF_{SW}^{Down}-LWP and ΔF_{SW}^{Up}-LWP). The 2D probability density (PD) is calculated for the paired datasets and defined as $PD_{ij} = 100\ \frac{N_{ij}}{N_t}$, where N_{ij} and N_t are the count number in the bin *ij* and the total count number ($N_t = \sum_{j=1}^{N}\sum_{i=1}^{M} N_{ij}$), respectively, with *M* and *N* being the total number of bins in LWP on one side, and in temperature or ΔF on the other side, respectively. So, for each value of T_j (within a 1°C-wide bin *j*) or ΔF_j (within a 5 W m^{-2}-wide bin *j*), a weighted average of LWP ($\overline{LWP_j}$) is calculated together with its associated weighted standard deviation ($\sigma_{LWP\,j}$), considering all the LWP_{ij} values (within 0.2 g m^{-2}-wide bins) from *i*=1 to *M*, with *M* the total number of LWP bins and w_{ij} the weight, namely the number of points ($w_{ij} = N_{ij}$), associated to the bin *ij*:

$$\overline{LWP_j} = \frac{\sum_{i=1}^{M} w_{ij}\, LWP_{ij}}{\sum_{i=1}^{M} w_{ij}} \tag{8}$$

and

$$\sigma_{LWP\,j} = \sqrt{\frac{\sum_{i=1}^{M} w_{ij}\,(LWP_{ij} - \overline{LWP_j})^2}{\sum_{i=1}^{M} w_{ij}}} \tag{9}$$

For each T and ΔF dataset, the distribution of the total count numbers N_{tj} per 1°C or 5 W m^{-2}-wide bin ($N_{tj} = \sum_{i=1}^{M} N_{ij}$ with $j = 1, \ldots, N$) can be fitted by a function $N(x)$, with $x =$ T or ΔF, based on 2 to 3 Gaussian distributions as:

313 $$N(x) = \sum_{k=1}^{2 \text{ or } 3} a_k \exp\left(-\frac{1}{2}\left(\frac{x-\mu_k}{\sigma_k}\right)^2\right) + c_0 \quad (10)$$

314 with a_k, μ_k and σ_k being the amplitude, the mean and the standard deviation of the k^{th} Gaussian
315 function and c_0 is a constant. We have used 0, 2 or 3 Gaussians for ΔF components and 3
316 Gaussians for T ("0" means that no Gaussian fit was meaningful). Table 2 lists all the fitted
317 parameters (a_k, μ_k, σ_k and c_0 with k = 0 to 3).

318 In the relationship between x (T or ΔF) and LWP, we have considered x_j (T_j or ΔF_j) to be
319 significant when:

320 $$|x_j - \mu_k| \leq \sigma_k \text{ for } k = 1 - 2 \text{ or } 3 \text{ (for } \Delta F) \text{ or } 1 - 3 \text{ (for } T) \quad (11)$$

321 and used for this significant point its average value and standard deviation, $\overline{LWP_j}$ and $\sigma_{LWP\,j}$,
322 respectively, with j = 1, …, N.

323 Finally, a logarithmic function of the form

324 $$x = \alpha + \beta \ln(\overline{LWP}) \quad (12)$$

325 has been fitted onto these significant points where the retrieved constants α and β are shown in
326 Table 3 for x being T, ΔF_{net}, ΔF_{LW}^{Down}, ΔF_{LW}^{Up}, ΔF_{SW}^{Down} and ΔF_{SW}^{Up}.

327

328 **4. Results**

329 *4.1. Temperature-Liquid Water Relationship in SLWCs*

330 The relationship between temperature and LWP within SLWCs over the 4-summer period
331 at Dome C is presented Figure 4 left in the form of a Probability Density (PD) that is the fraction
332 of points within each bin of 0.2 g m^{-2} width in LWP and 1.0°C width in temperature. It clearly
333 shows a net tendency for liquid water to increase with temperature, up to ~14 g m^{-2} in LWP and
334 -18°C in temperature, with two zones having a density as high as ~2%, at [0.5 g m^{-2}, -33°C]
335 and [1.5 g m^{-2}, -32°C]. We have performed a weighted average of the LWPs within each
336 temperature bin (Figure 4 centre). Then, we have fitted 3 Gaussian distributions to the count

numbers as a function of temperature (Figure 4 right). If we now only consider temperature bins within one-sigma of the centre of the Gaussian distributions, we can fit the following logarithmic relation of the temperature T as a function of LWP within the SLWC (Figure 4 centre):

$$T(LWP) = -33.8\ (\pm 1.5) + 6.5 \ln(LWP) \quad (13)$$

for $T \in [-36; -16]$ °C and $LWP \in [1.0; 14.0]$ g m^{-2}, with a validity range indicated by the 2 blue dashed lines ($\pm$1.5 °C) in Figure 4 centre. In other words, based on our study, we have a clear evidence that supercooled liquid water content exponentially increases with temperature. Considering the temperature vs. LWP relationship, the two main Gaussian distributions are centered around -28°C and -30°C, corresponding to temperatures usually encountered in Concordia whilst the third one, far much less intense, is centered around -18°C, probably the signature of very unusual events occurring in Concordia as the warm-moist events. Episodes of warm-moist intrusions exist above Concordia originated from mid-latitudes (Ricaud et al., 2017 and 2020) and are known as "atmospheric rivers" (Wille et al., 2019). Although they are infrequent, they can provide high values of temperature and LWP.

4.2. Radiative Forcing-Liquid Water Relationship in SLWC conditions

Although the amount of LWP is very low ($<$ 20 g m^{-2}) at Dome C compared to what can be measured and modelled (Lemus et al., 1997) in the Arctic (50 to 75 g m^{-2}) and at middle/tropical latitudes (100 to 150 g m^{-2}), we intended to estimate its impact on the cloud radiative forcing at Dome C. In Figures 5 to 9, the left panel presents the PDs of the cloud radiative forcing ΔF_{net} as a function of the LWP, and for the individual components that contribute to the cloud radiative forcing: ΔF_{LW}^{Down}, ΔF_{LW}^{Up}, ΔF_{SW}^{Down} and ΔF_{SW}^{Up}, respectively. The central panel shows, for the same parameters, the corresponding weighted average LWP within 5 W m^{-2}-wide bins of ΔF whereas the right panel shows the corresponding count number within

5 W m^{-2}-wide bins fitted by 2 or 3 Gaussian distributions (or no Gaussian distribution when it becomes impossible).

Based on our analysis, the relationship between ΔF_{net} (W m^{-2}) and the LWP (g m^{-2}) has been estimated as:

$$\Delta F_{net}(LWP) = -18.0\ (\pm 10.0)\ + 70.0 \ln(LWP) \quad (14)$$

for $\Delta F_{net} \in [0; 70]$ W m^{-2} and $LWP \in [1.2; 3.0]$ g m^{-2}, with a validity range indicated the two blue dashed lines ($\pm$10.0 W m^{-2}) in Figure 5 centre. Thus, for LWP greater than 1.2 g m^{-2}, our study clearly shows that the cloud radiative forcing induced by the presence of SLWCs above Concordia is positive and can reach 70 W m^{-2} for an LWP of 3.0 g m^{-2}.

The splitting of the cloud radiative forcing between each of its four components can be evaluated from their individual relationships with the LWP. These relations are gathered in Table 3, established from the plots presented in Figures 5 to 9. They are of the same form as for cloud radiative forcing, i.e. a logarithmic dependence on LWP. Table 3 presents the coefficients α and β of the logarithmic function $f(LWP) = \alpha + \beta \ln(LWP)$ for the temperature T or the radiation components ΔF, together with the valid range of these relations for $T, \Delta F$ and LWP. For the values presented in Table 3, our study clearly shows that SLWCs have a positive impact on ΔF_{LW}^{Down} increasing from 0 to 90 W m^{-2} for LWP ranging from 1.0 to 3.5 g m^{-2}, a negative impact on ΔF_{SW}^{Down} and ΔF_{SW}^{Up} decreasing from 0 to -130 and -110 W m^{-2}, respectively for LWP ranging from 1.5 to 4.0 g m^{-2}, and negligible impact ($\pm$5 W m^{-2}) on ΔF_{LW}^{Up} for LWP ranging from 0 to 6.5 g m^{-2}. Considering the absolute values of ΔF vs. LWP relationship (keeping aside ΔF_{LW}^{Up}), we have systematically the most intense Gaussian distributions centered at ~10 W m^{-2}, and the other ones centered at ~55 W m^{-2} and ~80 W m^{-2}.

To synthetize, our study showed that the major impact of SLWCs on net surface irradiance is an increase of downward longwave component (0 to 80 W m^{-2}), whereas it has a marginal impact on upward longwave component since this parameter is mainly dependent on T_s which

386 results from various meteorological forcings. In the presence of SLWC, the attenuation of
387 shortwave incoming irradiance (which can overpass 100 W m^{-2}) is almost compensated for by
388 the upward shortwave irradiance because of high values of surface albedo.

389 We can also estimate the sensitivity of the longwave component to temperature and
390 humidity by considering the values of the equivalent atmospheric emissivity ε_a used in the
391 equations 4-7. On the one side, the values of IWV observed at Dome C are very low even in
392 summer, typical summertime values are between 0.8 and 1.2 kg m^{-2} (Ricaud et al., 2020). This
393 corresponds to values of ε_a between 0.950 and 0.985, i.e. a relative variation of the order of
394 3.6%. On the other side, a variation ΔT of the screen-level air (surface) temperature T_a (T_s) has
395 a relative impact on the downwelling (upwelling) longwave irradiance of the order of $4\ \Delta T/T_a$
396 ($4\ \Delta T/T_s$), which amounts to around 1.6% per degree of ΔT. Given that observations of surface
397 and screen-level air temperatures reveal variations of several degrees, both in their diurnal cycle
398 and from a day to another, we can conclude that the impact of temperature on longwave
399 irradiance variations is larger than that of IWV.
400

401 **5. Discussion**

402 *5.1 Relation with critical temperature*

403 Our study shows that, above Concordia, there is an exponential dependence of LWP on both
404 temperature and cloud radiative forcing, that is to say supercooled liquid water exponentially
405 increases with temperature in the range -36°C to -16°C. This is in agreement with the outputs
406 from a simple model for thermodynamic properties of water from sub-zero temperatures up to
407 +100°C (Sippola and Taskinen, 2018). The model shows that the density ρ (g cm^{-3}) of liquid
408 water exponentially increases with temperature from -34°C to 0°C through the following
409 relationship:

410 $$\rho = \rho_0 \exp\{-T_c(A + B\varepsilon_0 + 2C\varepsilon_0^{1/2})\} \quad (15)$$

where ρ_0 = 1.007853 g cm^{-3}, A = 3.9744 10^{-4} K^{-1}, B = 1.6785 10^{-3} K^{-1}, and C = -7.8165 10^{-4} K^{-1}; T_c is the critical temperature (K) and ε_0 (unitless) is defined as:

$$\varepsilon_0 = \frac{T}{T_c} - 1 \quad (16)$$

where T is temperature in K. In thermodynamics, a critical point is the end point of a phase equilibrium curve. In our study, the liquid–ice boundary terminates at some critical temperature T_c. T_c is about 224.8 K if water is pure and free of nucleation nuclei. Sippola and Taskinen (2018) reviewed a value of T_c ~227-228 K (approx. -45°C) in the literature. This is also in agreement with the results from our study showing that, above Concordia, we could not observed SLWCs at temperatures less than -36°C consistent with the fact that the threshold temperature to get SLWCs should be around -39°C (see the discussions on errors in section 5.3).

5.2. Modelling SLWC

Previous studies have already underlined the difficulty to model the SLWC together with its impact on surface radiations. Modelling SLWCs over Antarctica is challenging because 1) operational observations are scarce since the majority of meteorological radiosondes are released from ground stations located at the coast and very few of them are maintained all year long, and satellite observations are limited to 60°S in geostationary orbit whilst, in a polar orbit, the number of available orbits does not exceed 15 per day, and 2) the model should provide a partition function favouring liquid water at the expense of ice for temperatures between -36°C and 0°C in order to calculate realistic SLW contents. Differences of 20 to 50 W m^{-2} in the net surface irradiance were found in the Arpege model (Pailleux et al., 2015) between clouds made of ice or liquid water during the summer 2018-2019 (Ricaud et al., 2020), differences that are very consistent with the results obtained in the present study. Although SLWCs are less present over the Antarctic Plateau than over the coastal region, their radiative impact is not negligible

435 and should be taken into account with great care in order to estimate the radiative budget of the
436 Antarctic continent in one hand, and, on the other hand, over the entire Earth.

437 *5.3. Errors*

438 Measurements of temperature, LWP, depolarization signal and surface irradiances F are
439 altered by random and systematic errors that may affect the relationships we have obtained
440 between LWP and either temperature or cloud radiative forcing ΔF_{net} and its individual
441 components. The temperature measured by HAMSTRAD below 1 km has been evaluated
442 against radiosonde coincident observations from 2009 to 2014 (Ricaud et al., 2015) and the
443 resulting bias is 0 to 2°C below 100 m and between -2 and 0°C between 100 and 1000 m.
444 SLWCs are usually located around 400-600 m above the ground where the cold bias can be
445 estimated to be about -1.0°C. The one-sigma (1-σ) RMS temperature error over a 7-min
446 integration time is 0.25°C in the PBL and 0.5°C in the free troposphere (Ricaud et al., 2015).
447 As a consequence, given the number of points used in the statistical analysis (>1000), the
448 random error on the weighted-average temperature is negligible (<0.02°C). The LWP random
449 and systematic errors are difficult to evaluate since there is no coincident external data to
450 compare with. Nevertheless, the 1-σ RMS error over a 7-min integration time can be estimated
451 to be 0.25 g m^{-2} giving a random error on the weighted average LWP less than 0.08 g m^{-2}. Based
452 on clear-sky observations, the positive bias can be estimated to be of the order of 0.4 g m^{-2}.
453 Theoretically, SLW should not exist at temperatures less than -39°C although it has been
454 observed in recent laboratory measurements down to -42.55°C (Goy et al., 2018). Using
455 equation (13) with an LWP bias of 0.4 g m^{-2} gives a temperature of -39.8°C (~0.8°C lower than
456 the theoretical limit of -39°C), so the biases estimated for temperature and LWP are very
457 consistent with theory.

458 The estimation of systematic and random errors on LIDAR backscattering and
459 depolarization signals and their impact on the attribution/selection of SLWC is not trivial. But

460 the most important point is to evaluate whether the observed cloud is constituted of purely liquid
461 or mixed-phase water. Even considering the backscatter intensity only, we could not exclude
462 that ice particles could have been present in the SLWC events investigated in 2018 (Ricaud et
463 al., 2020). Therefore, in the present analysis, although we made a great attention to diagnose
464 ice in the LIDAR cloud observations, we cannot totally exclude ice particles thus mixed-phase
465 parcels were actually present when we labelled the observed cloud as SLWCs.

466 The 4 instruments providing F_{LW}^{Down}, F_{LW}^{Up}, F_{SW}^{Down}, and F_{SW}^{Up} follow the rules of acquisition,
467 quality check and quality control of the BSRN (Driemel et al., 2018). These data are often
468 considered as a reference against which products based on satellite observations and radiative
469 transfer models (such as e.g. CERES) are validated (Kratz et al., 2020). In polar regions
470 (Lanconelli et al., 2011), F_{SW}^{Down} and F_{SW}^{Up} are expected to be affected by random errors up to
471 ±20 W m^{-2} while F_{LW}^{Down} are expected to be affected by random errors not greater than ±10 W
472 m^{-2} (Ohmura et al., 1998). As a consequence, given the large number of observations used per
473 5 W m^{-2}-wide bins (1000-3000), the random error on the weighted-average F is negligible (0.3
474 to 0.7 W m^{-2}) whatever the radiations considered, LW and SW.

475 Finally, another source of error comes from 1) the geometry of observation and 2) the
476 discontinuous SLWC layer. Firstly, LIDAR is almost zenith pointing, HAMSTRAD makes a
477 scan in the East direction (from 10° elevation to zenith), whilst the BSRN radiometers detect
478 the radiation in a 2π-steradians field of view (3D configuration). That is to say, in our analysis,
479 the whole sky contributes to the radiation whilst only the cloud at zenith (1D configuration) and
480 on the East direction (2D configuration) is observed by the LIDAR and HAMSTRAD,
481 respectively. Secondly, SLWCs cannot be considered as uniform in the whole (see e.g. broken
482 cloud fields in Figure 2).

483 *5.4. Other clouds*

Although the method we have developed to select the SLWCs has been validated using the amount of LWP and, in another study, using space-borne observations (Ricaud et al., 2020), we cannot rule out that, associated with the SLW droplets, are also ice particles, that is clouds are constituted of a mixture of liquid and solid water. Statistics of ice and mixed-phase clouds over the Antarctic Plateau have been performed by Cossich et al. (2021) revealing mean annual occurrences of 72.3 %, 24.9 %, and 2.7 % for clear sky, ice clouds, and mixed-phase clouds, respectively. Generally, mixed-phase clouds are a superposition of a lower layer being made of liquid water and an upper layer being made of solid water (see Fig. 12.3 from Lamb and Verlinde, 2011). These mixed-layer clouds do not significantly modify the relationship between temperature and LWP because 1) SLW observations from HAMSTRAD are only sensitive to water in liquid phase and 2) temperature from HAMSTRAD is selected at times and vertical heights where the LIDAR depolarization signal is very low (<5%). Although we have verified that pure ice clouds were not selected by our method, we cannot differentiate mixed-phase clouds from purely SLWCs.

Furthermore, we already have noticed that SLWCs developed at the top of the PBL (Ricaud et al., 2020) in the "entrainment zone" and maintained in the "capping inversion zone", following the terminology of Stull (1988), at a height ranging from 100 to 1000 m above ground level. Nevertheless, at 00:00-06:00 LT when the sun is at low elevation above the horizon (24-h polar day), the PBL may collapse down to a very low height ranging 20-50 m. In this configuration, it is hard to differentiate from LIDAR observations between a SLWC and a fog episode, although the LIDAR can measure depolarization (but not backscatter) down to approximately 10-30 m above the ground (Figure S3 in Chen et al., 2017), so that we can distinguish liquid/frozen clouds very close to the ground.

Finally, we cannot rule out that, above the SLWCs that are actually observed by both LIDAR and HAMSTRAD, other clouds might be present, as e.g. cirrus clouds constituted of

ice crystals. These mid-to-upper tropospheric clouds cannot be detected by HAMSTRAD (no sensitivity to ice crystals). In the presence of SLWCs either low in altitude or optically thick, the LIDAR backscatter signal is decreased in order to avoid saturation and the signal from upper layers is thus almost cancelled. These mid-to-high-altitude clouds are sensed by the BSRN instruments and surface irradiance can be affected in this configuration. Based on the presence of cirrus clouds before or after the SLWCs (and sometimes during the SLWCs if optically thin), we can estimate that the number of days when SLWCs and cirrus clouds are simultaneously present to cover less than 10% of our period of interest.

5.5. Sastrugi effect on the surface albedo

Sastrugi are features formed by erosion of snow by wind. They are found in polar regions, and in snowy, wind-swept areas of temperate regions, such as frozen lakes or mountain ridges. Sastrugi are distinguished by upwind-facing points, resembling anvils, which move downwind as the surface erodes.

Figure 10 shows the BSRN surface albedo averaged over the five cloud-free days (2 and 19 December 2018; 3, 17 and 26 December 2021) showing a clear diurnal signal with a maximum of 0.85 from 10:00 to 14:00 UTC (from 18:00 to 22:00 LT) and a minimum of 0.70 from 19:00 to 23:00 UTC (from 03:00 to 07:00 LT). The large diurnal signal present in the observed surface albedo is likely the signature of 1) the sastrugi orientation and also 2) the sun zenith angle which impacts on the surface albedo even with a flat snow surface (Gardner and Sharp, 2010). Note that the surface albedo of snow under cloudy conditions may differ from the surface albedo under cloud-free conditions (e.g., Gardner and Sharp, 2010; Stapf et al., 2020). The BSRN F_{SW}^{Up} sensor has a circular footprint. For a sensor installed at a height h above the ground, 90% of the signal comes from an area at the surface closer than 3.1 h (Kassianov et al., 2014). Since at Dome-C the instrument is installed at a height of 2-3 m, the albedo is thus determined by the surface elements in the immediate vicinity (a few meters) of the sensor.

We have fitted the averaged cloud-free BSRN surface albedo with the sum of two sine functions, imposing periods of 24 and 12 hours (Figure 10) together with the residuals between the averaged surface albedo and the fitted function. We can state that the sastrugi effect on the observed cloud-free surface albedo at Concordia is successfully fitted by two sine functions of 24h and 12h periods to within 0.003 mean absolute error, with a coefficient of determination R^2 equal to 0.993 and a root mean square error of 0.0004.

Moreover, we have considered all the BSRN observations in Decembers 2018, 2019, 2020 and 2021 to calculate the albedo (Figure 11), and we have superimposed the fitted trigonometric function as described in Figure 10. The presence of clouds is well highlighted by observations that depart from the fitted function whilst, during periods of clear-sky conditions, BSRN albedos coincide well with the fitted function. To conclude, the surface albedo at Concordia should be treated considering sastrugi effect.

5.6. Maximum SLWC Radiative Forcing over Antarctica

Based on 2007-2010 reanalyses, observations and climate models (Lenaerts et al., 2017), LWP over Antarctica is on average less than 10 g m^{-2}, with slightly larger values in summer than in winter by 2 to 5 g m^{-2}. Over Western Antarctica, LWPs are larger (20 to 40 g m^{-2}) than over Eastern Antarctica (0 to 10 g m^{-2}). As a consequence, LWPs observed at Concordia are consistent with values observed over the Eastern Plateau, with a factor 2 to 4 smaller than those observed over the Western continent. Based on our results and on the observed cloud fraction (η_{CF}) of SLWCs over Antarctica for different seasons (Listowski et al., 2019), we can estimate the maximum SLWC radiative forcing at the scale of the Antarctic continent ($\Delta F_{Net-Ant}^{max}$) from the maximum of ΔF_{net} ($\Delta F_{Net}^{max} = 70$ W m^{-2}) computed in our study:

$$\Delta F_{Net-Ant}^{max} = \eta_{CF} \times \Delta F_{Net}^{max} \quad (17)$$

Equation (17) assumes a linear dependence between cloud fraction and cloud radiative forcing although, in nature, there could be three-dimensional radiation effects. In summer, η_{CF} is

559 varying from 5% in Eastern Antarctica to 40% in Western Antarctica whilst, in winter, it is
560 varying from 0% in Eastern Antarctica to 20% in Western Antarctica (Listowski et al., 2019).
561 In December, if we consider η_{CF} for SLW-containing cloud (that is to say both mixed-phase
562 cloud and unglaciated SLW cloud consistent with our study), we find for a lower-level altitude
563 cut-off of 0, 500 and 1000 m (Figure B1 in Listowski et al., 2019), a maximum SLWC radiative
564 forcing $\Delta F_{Net-Ant}^{max}$ over Antarctica of about 12 W m^{-2}, 10 W m^{-2} and 7 W m^{-2}, respectively. We
565 now separate the Eastern elevated Antarctic Plateau from the Western Antarctica (Figure 5 in
566 Listowski et al., 2019) for the 4 seasons. Over Eastern Antarctica, we find that $\Delta F_{Net-Ant}^{max} = 0.7$
567 to 7.0 W m^{-2} in December-January-February (DJF) and 0 to 3.5 W m^{-2} for the remaining
568 seasons. Over Western Antarctica, the maximum radiative impact is much more intense because
569 of higher temperatures and lower elevations compared to the Eastern Antarctic Plateau:
570 $\Delta F_{Net-Ant}^{max} =$ 17.5 to 40.0 W m^{-2} in DJF (40 W m^{-2} over the Antarctica Peninsula); 10.5 to 28.0
571 W m^{-2} in March-April-May; 3.5 to 14.0 W m^{-2} in June-July-August; and 7.0 to 17.5 W m^{-2} in
572 September-October-November. To summarize, the maximum SLWC radiative forcing over
573 Western Antarctica (0 to 40 W m^{-2}) is estimated to 3 to 5 times larger compared to the one over
574 the Eastern Antarctic Plateau (0 to 7 W m^{-2}), maximizing during the summer season.
575
576 **6. Conclusions**
577 Combining the observations of temperature, water vapour and liquid water path from a
578 ground-based microwave radiometer, backscattering and depolarization from a ground-based
579 LIDAR, screen-level air temperature and surface radiations at long and short wavelengths, our
580 analysis has been able to evaluate the presence of supercooled liquid water clouds over the
581 Dome C station in summer. Focusing on the month of December in 2018-2021, we established
582 that in SLWCs temperature logarithmically increases from -36.0°C to -16.0°C when LWP
583 increases from 1.0 to 14.0 g m^{-2}. We have also evaluated that SLWCs have a positive cloud

radiative forcing, which logarithmically increases from 0.0 to 70.0 W m^{-2} when LWP increases from 1.2 to 3.5 g m^{-2}. Our study clearly shows that SLWCs have a positive impact on ΔF_{LW}^{Down} increasing from 0 to 90 W m^{-2} for LWP ranging from 1.0 to 3.5 g m^{-2}, a negligible impact (±5 W m^{-2}) on ΔF_{LW}^{Up} for LWP ranging from 0 to 6.5 g m^{-2}, and a negative (but quite offsetting) impact on each of the two terms ΔF_{SW}^{Down} and ΔF_{SW}^{Up} which decrease from 0 to -130 and -110 W m^{-2}, respectively for LWP ranging from 1.5 to 4.0 g m^{-2}. This means that the SLWC radiative forcing is mainly driven by the downward surface irradiance since the attenuation of shortwave incoming irradiance is almost compensated for by the upward shortwave irradiance because of high values of surface albedo.

Finally, extrapolating our results of the SLWC radiative forcing from the Dome C station to the Antarctic continent shows that the maximum SLWC radiative forcing is not greater than 7.0 W m^{-2} over the Eastern Antarctic Plateau but 2 to 3 times larger (up to 40 W m^{-2}) over Western Antarctica, maximizing over in summer season and over the Antarctic Peninsula. This stresses the importance of accurately modelling SLWCs when calculating the Earth energy budget to adequately forecast the Earth climate evolution, especially since the climate is rapidly changing in Antarctica, as illustrated by the surface temperature record of -12°C recently observed in March 2022 at the Concordia station and largely publicized worldwide (see e.g. https://www.9news.com.au/world/antarctica-heatwave-extreme-warm-weather-recorded-concordia-research-station/3364dd91-2051-4df5-8cfc-5f2819058604).

Data availability

HAMSTRAD data are available at http://www.cnrm.meteo.fr/spip.php?article961&lang=en (last access: 27 November 2023). The tropospheric depolarization LIDAR data are reachable at http://lidarmax.altervista.org/lidar/home.php (last access: 27 November 2023). Radiosondes are available at http://www.climantartide.it (last access: 27 November 2023). Screen-level air

temperature from AWS can be obtained from the ftp server (https://amrc.ssec.wisc.edu/data/archiveaws.html) (last access: 27 November 2023). BSRN data can be obtained from the ftp server (https://bsrn.awi.de/data/data-retrieval-via-ftp/) (last access: 27 November 2023).

Author contribution

PR, MDG, and AL provided the observational data. PR developed the methodology. All the co-authors participated in the data analysis and in the data interpretation. PR prepared the manuscript with contributions from all co-authors.

Competing interests

The authors declare that they have no conflict of interest.

Acknowledgments

The present research project Water Budget over Dome C (H2O-DC) has been approved by the Year of Polar Prediction (YOPP) international committee. The HAMSTRAD programme (910) was supported by the French Polar Institute, Institut polaire français Paul-Emile Victor (IPEV), the Institut National des Sciences de l'Univers (INSU)/Centre National de la Recherche Scientifique (CNRS), Météo-France and the Centre National d'Etudes Spatiales (CNES). The permanently manned Concordia station is jointly operated by IPEV and the Italian Programma Nazionale Ricerche in Antartide (PNRA). The tropospheric LIDAR operates at Dome C from 2008 within the framework of several Italian national (PNRA) projects. We would like to thank all the winterover personnel who worked at Dome C on the different projects: HAMSTRAD, aerosol LIDAR and BSRN. We would like to thank the three anonymous reviewers for their beneficial comments.

634

635 **References**

636 Bergeron, T., 1928: Über die dreidimensional verknüpfende Wetteranalyse. – Geophys. Norv.

637 Branch, M. A., T. F. Coleman, and Y. Li: A Subspace, Interior, and Conjugate Gradient Method
638 for Large-Scale Bound-Constrained Minimization Problems, SIAM Journal on Scientific
639 Computing, 21, 1, 1-23, 1999.

640 Bromwich, D. H., Nicolas, J. P., Hines, K. M., Kay, J. E., Key, E. L., Lazzara, Lubin, D.,
641 McFarquhar, G. M., Gorodetskaya, I. V., Grosvenor, D. P., Lachlan-Cope, T., and van
642 Lipzig, N. P. M.: Tropospheric clouds in Antarctica, Rev. Geophys., 50, RG1004,
643 https://doi.org/10.1029/2011RG000363, 2012.

644 Bromwich, D. H., Otieno, F. O., Hines, K. M., Manning, K. W., and Shilo, E.: Comprehensive
645 evaluation of polar weather research and forecasting model performance in the Antarctic, J.
646 Geophys. Res.-Atmos., 118, 274–292, 2013.

647 Chen, X., Virkkula, A., Kerminen, V.-M., Manninen, H. E., Busetto, M., Lanconelli, C., Lupi,
648 A., Vitale, V., Del Guasta, M., Grigioni, P., Väänänen, R., Duplissy, E.-M., Petäjä, T., and
649 Kulmala, M.: Features in air ions measured by an air ion spectrometer (AIS) at Dome C,
650 Atmos. Chem. Phys., 17, 13783–13800, https://doi.org/10.5194/acp-17-13783-2017, 2017.

651 Cossich, W., Maestri, T., Magurno, D., Martinazzo, M., Di Natale, G., Palchetti, L., Bianchini,
652 G., and Del Guasta, M.: Ice and mixed-phase cloud statistics on the Antarctic Plateau,
653 Atmos. Chem. Phys., 21, 13811–13833, https://doi.org/10.5194/acp-21-13811-2021, 2021.

654 Driemel, A., Augustine, J., Behrens, K., Colle, S., Cox, C., Cuevas-Agulló, E., Denn, F. M.,
655 Duprat, T., Fukuda, M., Grobe, H., Haeffelin, M., Hodges, G., Hyett, N., Ijima, O., Kallis,
656 A., Knap, W., Kustov, V., Long, C. N., Longenecker, D., Lupi, A., Maturilli, M., Mimouni,
657 M., Ntsangwane, L., Ogihara, H., Olano, X., Olefs, M., Omori, M., Passamani, L., Pereira,
658 E. B., Schmithüsen, H., Schumacher, S., Sieger, R., Tamlyn, J., Vogt, R., Vuilleumier, L.,

Xia, X., Ohmura, A., and König-Langlo, G.: Baseline Surface Radiation Network (BSRN): structure and data description (1992–2017), Earth Syst. Sci. Data, 10, 1491–1501, https://doi.org/10.5194/essd-10-1491-2018, 2018.

Dupont, J.C., Haeffelin, M., Drobinski, P. and Besnard, T.: Parametric model to estimate clear-sky longwave irradiance at the surface on the basis of vertical distribution of humidity and temperature. Journal of Geophysical Research: Atmospheres, 113(D7), https://doi.org/10.1029/2007JD009046, 2008.

Dutton, E.G., Farhadi, A., Stone, R.S., Long, C.N. and Nelson, D.W.: Long-term variations in the occurrence and effective solar transmission of clouds as determined from surface-based total irradiance observations. Journal of Geophysical Research: Atmospheres, 109(D3), https://doi.org/10.1029/2003JD003568, 2004.

Findeisen, W., 1938: Kolloid-meteorologische Vorgänge bei Niederschlagsbildung. Meteorol. Z. 55, 121–133. (translated and edited by Volken, E., A.M. Giesche, S. Brönnimann. – Meteorol. Z. 24 (2015), DOI:10.1127/metz/2015/0675).

Gardner, A.S. and Sharp, M.J.: A review of snow and ice albedo and the development of a new physically based broadband albedo parameterization. Journal of Geophysical Research: Earth Surface, 115(F1), 2010.

Goy, C., Potenza, M. A., Dedera, S., Tomut, M., Guillerm, E., Kalinin, A., Voss, K.-O., Schottelius, A., Petridis, N., Prosvetov, A., Tejeda, G., Fernández, J. M., Trautmann, C., Caupin, F., Glasmacher, U., and Grisenti, R. E.: Shrinking of rapidly evaporating water microdroplets reveals their extreme supercooling, Phys. Rev. Lett., 120, 015501, https://doi.org/10.1103/PhysRevLett.120.015501, 2018.

Grazioli, J., Genthon, C., Boudevillain, B., Duran-Alarcon, C., Del Guasta, M., Madeleine, J.-B., and Berne, A.: Measurements of precipitation in Dumont d'Urville, Adélie Land, East

683 Antarctica, The Cryosphere, 11, 1797–1811, https://doi.org/10.5194/tc-11-1797-2017,
684 2017.
685 Grosvenor, D. P., Choularton, T. W., Lachlan-Cope, T., Gallagher, M. W., Crosier, J., Bower,
686 K. N., Ladkin, R. S., and Dorsey, J. R.: In-situ aircraft observations of ice concentrations
687 within clouds over the Antarctic Peninsula and Larsen Ice Shelf, Atmos. Chem. Phys., 12,
688 11275–11294, https://doi.org/10.5194/acp-12-11275-2012, 2012.
689 Hogan, R. J. and Illingworth, A. J.: The effect of specular reflection on spaceborne lidar
690 measurements of ice clouds, Report of the ESA Retrieval algorithm for EarthCARE project,
691 5 pp., 2003.
692 Kassianov E, Barnard J, Flynn C, Riihimaki L, Michalsky J, Hodges G (2014) Areal-averaged
693 spectral surface albedo from ground-based transmission data alone: toward an operational
694 retrieval. Atmosphere 5:597–621. https://doi.org/10.3390/atmos503059)
695 King, J. C., Argentini, S. A., and Anderson, P. S.: Contrasts between the summertime surface
696 energy balance and boundary layer structure at Dome C and Halley stations, Antarctica, J.
697 Geophys. Res.-Atmos., 111, D02105, https://doi.org/10.1029/2005JD006130, 2006.
698 King, J. C., Gadian, A., Kirchgaessner, A., Kuipers Munneke, P., Lachlan-Cope, T. A., Orr, A.,
699 Reijmer, C., Broeke, M. R., van Wessem, J. M., and Weeks, M.: Validation of the
700 summertime surface energy budget of Larsen C Ice Shelf (Antarctica) as represented in
701 three high-resolution atmospheric models, J. Geophys. Res.-Atmos., 120, 1335–1347,
702 https://doi.org/10.1002/2014JD022604, 2015.
703 Kratz, D. P., Gupta, S. K., Wilber, A. C., and Sothcott, V. E.: Validation of the CERES Edition-
704 4A Surface-Only Flux Algorithms, J. Appl. Meteorol. Clim., 59, 281–295,
705 https://doi.org/10.1175/JAMC-D-19-0068.1, 2020.
706 Lachlan-Cope, T.: Antarctic clouds, Polar Res., 29, 150–158, 2010.

Lachlan-Cope, T., Listowski, C., and O'Shea, S.: The microphysics of clouds over the Antarctic Peninsula – Part 1: Observations, Atmos. Chem. Phys., 16, 15605–15617, https://doi.org/10.5194/acp-16-15605-2016, 2016.

Lamb, D., and J. Verlinde: Physics and chemistry of clouds. Cambridge University Press, 2011.

Lanconelli, C., Busetto, M., Dutton, E. G., König-Langlo, G., Maturilli, M., Sieger, R., Vitale, V., and Yamanouchi, T.: Polar baseline surface radiation measurements during the International Polar Year 2007–2009, Earth Syst. Sci. Data, 3, 1–8, https://doi.org/10.5194/essd-3-1-2011, 2011.

Lawson, R. P. and Gettelman, A.: Impact of Antarctic mixed-phase clouds on climate, P. Natl. Acad. Sci. USA, 111, 18156–18161, 2014.

Legrand, M., Yang, X., Preunkert, S., and Therys, N.: Year-round records of sea salt, gaseous, and particulate inorganic bromine in the atmospheric boundary layer at coastal (Dumont d'Urville) and central (Concordia) East Antarctic sites, J. Geophys. Res. Atmos., 121, 997–1023, https://doi.org/10.1002/2015JD024066, 2016.

Lemus, L., Rikus, L., Martin, C., and Platt, R.: Global cloud liquid water path simulations. J. Climate, 10(1), 52-64, 1997.

Lenaerts, J. T., Van Tricht, K., Lhermitte, S. and L'Ecuyer, T. S.: Polar clouds and radiation in satellite observations, reanalyses, and climate models, Geophysical Research Letters, 44(7), 3355-3364, 2017.

Listowski, C. and Lachlan-Cope, T.: The microphysics of clouds over the Antarctic Peninsula – Part 2: modelling aspects within Polar WRF, Atmos. Chem. Phys., 17, 10195–10221, https://doi.org/10.5194/acp-17-10195-2017, 2017.

Listowski, C., Delanoë, J., Kirchgaessner, A., Lachlan-Cope, T., and King, J.: Antarctic clouds, supercooled liquid water and mixed phase, investigated with DARDAR: geographical and

731 seasonal variations, Atmos. Chem. Phys., 19, 6771–6808, https://doi.org/10.5194/acp-19-
732 6771-2019, 2019.
733 Lubin, D., Chen, B., Bromwich, D. H., Somerville, R. C., Lee, W. H., and Hines, K. M.: The
734 Impact of Antarctic Cloud Radiative Properties on a GCM Climate Simulation, J. Climate,
735 11, 447-462, 1998.
736 Mishchenko, M. I., Hovenier, J. W., and Travis, L. D. (Eds.): Light Scattering by Nonspherical
737 Particles: Theory, Measurements, and Applications, Academic Press, chap. 14, 393–416,
738 2000.
739 Ohmura, A., Dutton,E. G., Forgan, B., Fröhlich, C., Gilgen, H., Hegner, H., Heimo, A., König-
740 Langlo, G., McArthur, B., Müller, G., Philipona, R., Pinker, R., Whitlock, C. H., Dehne,
741 K., and Wild, M.: Baseline Surface Radiation Network (BSRN/WCRP): New precision
742 radiometry for climate research, B. Am. Meteorol. Soc., 79(10), 2115-2136, 1998.
743 O'Shea, S. J., Choularton, T. W., Flynn, M., Bower, K. N., Gallagher, M., Crosier, J., Williams,
744 P., Crawford, I., Flem- ing, Z. L., Listowski, C., Kirchgaessner, A., Ladkin, R. S., and
745 Lachlan-Cope, T.: In situ measurements of cloud microphysics and aerosol over coastal
746 Antarctica during the MAC campaign, Atmos. Chem. Phys., 17, 13049–13070,
747 https://doi.org/10.5194/acp-17-13049-2017, 2017.
748 Pailleux, J., Geleyn, J.-F., El Khatib, R., Fischer, C., Hamrud, M., Thépaut, J.-N., Rabier, F.,
749 Andersson, E., Salmond, D., Burridge, D., Simmons, A., and Courtier, P.: Les 25 ans du
750 système de prévision numérique du temps IFS/Arpège, La Météorologie, 89, 18–27,
751 https://doi.org/10.4267/2042/56594, 2015.
752 Ricaud, P., Gabard, B., Derrien, S., Chaboureau, J.-P., Rose, T., Mombauer, A. and Czekala,
753 H.: HAMSTRAD-Tropo, A 183-GHz Radiometer Dedicated to Sound Tropospheric Water
754 Vapor Over Concordia Station, Antarctica, IEEE T. Geosci. Remote, 48, 1365–1380, doi:
755 10.1109/TGRS.2009.2029345, 2010a.

Ricaud, P., Gabard, B., Derrien, S., Attié, J.-L., Rose, T., and Czekala, H.: Validation of tropospheric water vapor as measured by the 183-GHz HAMSTRAD Radiometer over the Pyrenees Mountains, France, IEEE T. Geosci. Remote, 48, 2189–2203, 2010b.

Ricaud, P., Genthon, C., Durand, P., Attié, J.-L., Carminati, F., Canut, G., Vanacker, J.-F., Moggio, L., Courcoux, Y., Pellegrini, A., and Rose, T.: Summer to Winter Diurnal Variabilities of Temperature and Water Vapor in the lowermost troposphere as observed by the HAMSTRAD Radiometer over Dome C, Antarctica, Bound.-Lay. Meteorol., 143, 227–259, doi:10.1007/s10546-011-9673-6, 2012.

Ricaud, P., Grigioni, P., Zbinden, R., Attié, J.-L., Genoni, L., Galeandro, A., Moggio, A., Montaguti, S., Petenko, I., and Legovini, P.: Review of tropospheric temperature, absolute humidity and integrated water vapour from the HAMSTRAD radiometer installed at Dome C, Antarctica, 2009–14, Antarct. Sci., 27, 598-616, doi:10.1017/S0954102015000334, 2015.

Ricaud, P., Bazile, E., del Guasta, M., Lanconelli, C., Grigioni, P., and Mahjoub, A.: Genesis of diamond dust, ice fog and thick cloud episodes observed and modelled above Dome C, Antarctica, Atmos. Chem. Phys., 17, 5221-5237, https://doi.org/10.5194/acp-17-5221-2017, 2017.

Ricaud, P., Del Guasta, M., Bazile, E., Azouz, N., Lupi, A., Durand, P., Attié, J.-L., Veron, D., Guidard, V., and Grigioni, P.: Supercooled liquid water cloud observed, analysed, and modelled at the top of the planetary boundary layer above Dome C, Antarctica, Atmos. Chem. Phys., 20, 4167–4191, https://doi.org/10.5194/acp-20-4167-2020, 2020.

Sippola, H., and Taskinen, P.: Activity of supercooled water on the ice curve and other thermodynamic properties of liquid water up to the boiling point at standard pressure, J. Chem. Engineer. Data, 63(8), 2986-2998, 2018.

780 Stapf, J., Ehrlich, A., Jäkel, E., Lüpkes, C., and Wendisch, M.: Reassessment of shortwave
781 surface cloud radiative forcing in the Arctic: consideration of surface-albedo–cloud
782 interactions, Atmos. Chem. Phys., 20, 9895–9914, https://doi.org/10.5194/acp-20-9895-
783 2020, 2020.
784 Storelvmo, T. and Tan, I.: The Wegener–Bergeron–Findeisen process—Its discovery and vital
785 importance for weather and climate, Meteor. Z, 24, 455-461, 2015.
786 Stull, R. B.: An introduction to boundary layer meteorology, Kluwer Academic Publisher,
787 1988.
788 Tomasi, C., Petkov, B., Mazzola, M., Ritter, C., di Sarra, A., di Iorio, T., and del Guasta, M.:
789 Seasonal variations of the relative optical air mass function for background aerosol and thin
790 cirrus clouds at Arctic and Antarctic sites, Remote Sensing, 7(6), 7157-7180, 2015.
791 Wegener, A. 1911. Thermodynamik der Atmosphäre. – Leipzig, Germany: Barth.
792 Wille, J. D., Favier, V., Dufour, A., Gorodetskaya, I. V., Turner, J., Agosta, C. and Codron, F.:
793 West Antarctic surface melt triggered by atmospheric rivers, Nature Geoscience, 12(11),
794 911-916, 2019.
795 Young, G., Lachlan-Cope, T., O'Shea, S. J., Dearden, C., Listowski, C., Bower, K. N.,
796 Choularton, T. W., and Gallagher, M. W.: Radiative effects of secondary ice enhancement
797 in coastal Antarctic clouds, Geophys. Res. Lett., 46, 2312–2321,
798 https://doi.org/10.1029/2018GL080551, 2019.
799

Tables

Table 1. Cloud-free periods in December 2018-2021 detected from the LIDAR depolarization observations at Concordia. Time is in UTC. MM-NN means from MM (included) hour UTC to NN (excluded) hour UTC. "X" means no cloud-free period during that day. "ND" means no LIDAR data available. Bold cases mean that cloud-free irradiance calculations are impossible due to lack of some data (LIDAR, HAMSTRAD, BSRN or AWS).

Days	2018	2019	2020	2021
01	0-24	**9-18**	**ND**	**9-16**
02	0-21	**13-17**	**ND**	**7-8**
03	0-24	**6-16**	**ND**	**6-24**
04	X	**11-16**	**ND**	**0-24**
05	X	6-16	**3-16**	**12-19**
06	3-6	0-13	9-13	**2-12**
07	**1-16**	X	X	**0-24**
08	3-15	X	1-2	**0-10**
09	**2-16**	X	**4-14**	**10-17**
10	0-3	X	X	**ND**
11	X	4-17	0-1	**ND**
12	X	X	20-22	**ND**
13	11-13	10-14	0-12	X
14	22-24	17-18	X	5-12 & 17-20
15	4-8	**22-23**	X	3-6
16	**15-18**	X	**6-8**	11-24
17	18-19	**ND**	X	0-24
18	1-17	**ND**	16-17	0-3
19	0-24	**ND**	7-9 & 11-13	20-23
20	**0-12**	**ND**	20-22	16-19
21	X	**ND**	20-21	X
22	9-16	**ND**	ND	12-15
23	1-4	**ND**	**14-20**	X
24	X	**ND**	**11-14**	0-6
25	X	**ND**	9-15	**20-24**
26	12-18	**ND**	0-16 & 18-22	0-24
27	**10-11**	**ND**	0-2	0-4
28	**0-6**	**ND**	0-17	**10-14**
29	**X**	**ND**	0-18	**X**
30	**X**	**ND**	**7-24**	**X**
31	**10-12**	**ND**	0-18	**X**

808

809 **Table 2.** Gaussian functions fitted to the $N(x)$ function for $x = T$ (°C) or ΔF (W m^{-2}). Units of

810 a_1, a_2, a_3, and c_0 are in count number for T and ΔF; units of μ_1, μ_2, μ_3, σ_1, σ_2, and σ_3 are in

811 °C for T and in W m^{-2} for ΔF.

x	a_1	μ_1	σ_1	a_2	μ_2	σ_2	a_3	μ_3	σ_3	c_0
T	15.0 10^3	-31.5	1.45	5.0 10^3	-28.0	1.65	0.5 10^3	-19.0	2.5	-9.1 10^{-6}
ΔF_{net}	371.7	10.0	11.5	74.6	37.6	21.1	220.8	57.5	14.1	-10.2
ΔF_{LW}^{Down}	415.5	10.0	10.4	189.5	53.7	24.2	227.1	82.9	7.0	-18.5
ΔF_{LW}^{Up}	-	-	-	-	-	-	-	-	-	-
ΔF_{SW}^{Down}	190.5	-10.1	17.2	113.0	-80.0	54.6	-	-	-	-1.9
ΔF_{SW}^{Up}	282.4	-10.1	12.8	133.8	-75.0	41.8	-	-	-	8.3

812

813

Table 3. Coefficients of the relations $f(LWP) = \alpha + \beta \ln(LWP)$ for the temperature T or cloud radiative forcing (ΔF_{net}) and the individual components (ΔF_{LW}^{Down}, ΔF_{LW}^{Up}, ΔF_{SW}^{Down} and ΔF_{SW}^{Up}). Units of T and ΔF, as well as of their corresponding "α" values are in °C and W m^{-2}, respectively; units of β are in °C g^{-1} m^2 for T and in W g^{-1} for ΔF; units of LWP are in g m^{-2}. The last column shows the range of LWP values for which the relation is valid. $\alpha \pm \delta\alpha$ corresponds to the range of α values where the relationship is valid.

$f(LWP)$	$\alpha \pm \delta\alpha$	β	**Valid range for T or ΔF**	**Valid range for LWP**
T	-33.8 ± 1.5	6.5	$[-36; -16]$	[1.0; 14.0]
ΔF_{net}	-18.0 ± 10.0	70.0	[0; 70]	[1.2; 3.5]
ΔF_{LW}^{Down}	5.0 ± 15.0	65.0	[0; 90]	[1.0; 3.5]
ΔF_{LW}^{Up}	0 ± 5.0	0.0	$[-5; 5]$	[0.0; 6.5]
ΔF_{SW}^{Down}	30.0 ± 30.0	-130.0	$[-130; 0]$	[1.5; 4.0]
ΔF_{SW}^{Up}	30.0 ± 30.0	-110.0	$[-110; 00]$	[1.5; 4.0]

Figures

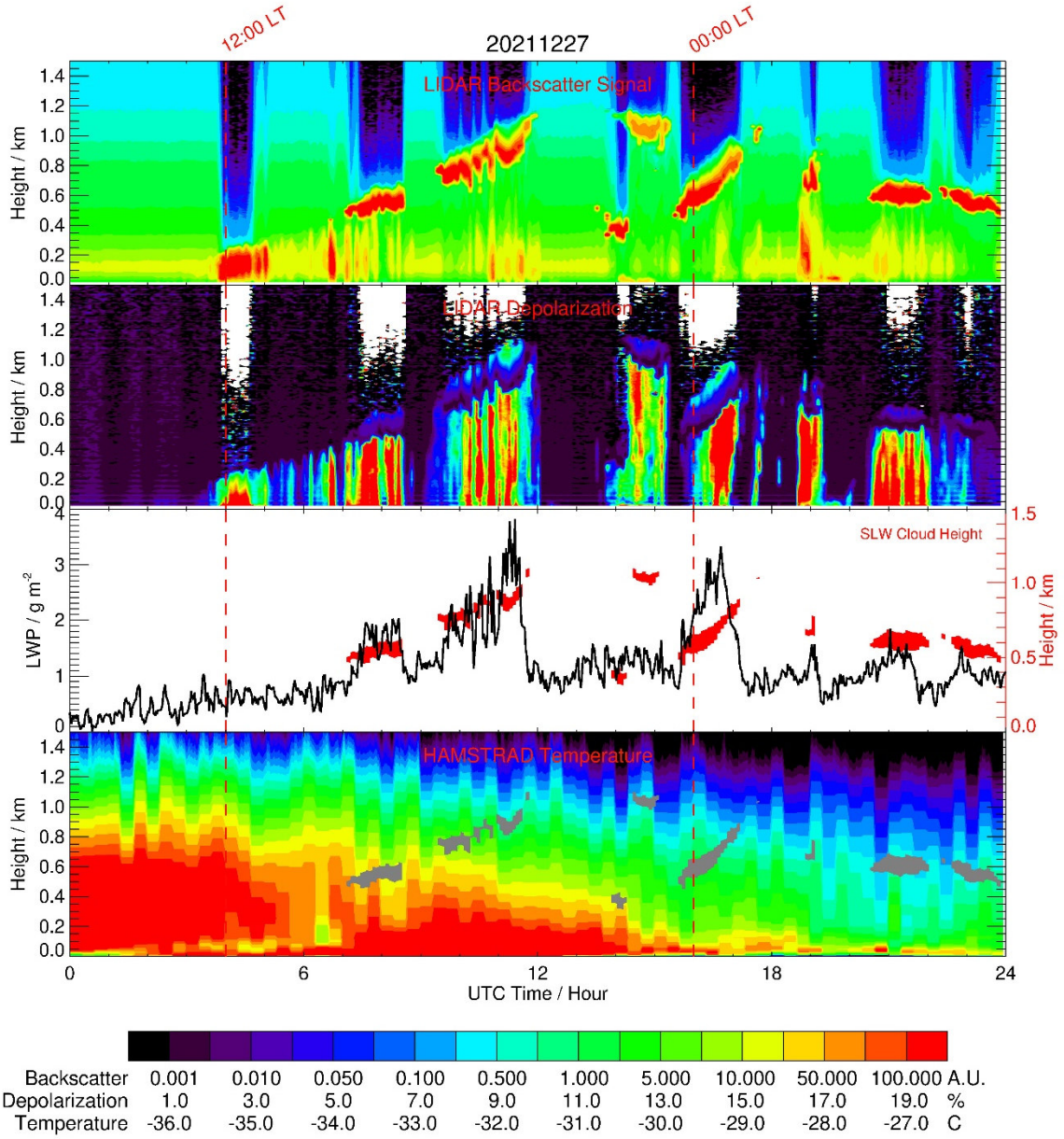

Figure 1: (From top to bottom): Time evolution (UTC, hour) of the LIDAR backscattering signal, the LIDAR depolarization signal, the HAMSTRAD LWP and the HAMSTRAD temperature profile measured on 27 December 2021. The time evolution of the SLW cloud (as diagnosed by a backscattering value > 60 A.U. and a depolarization value < 5%) is highlighted by the red and grey areas in the third and the forth panel from the top, respectively. The height above the ground is shown on the third panel from the top with the y-axis on the right. The 00:00 and 12:00 local times (LT) are highlighted by 2 vertical dashed lines.

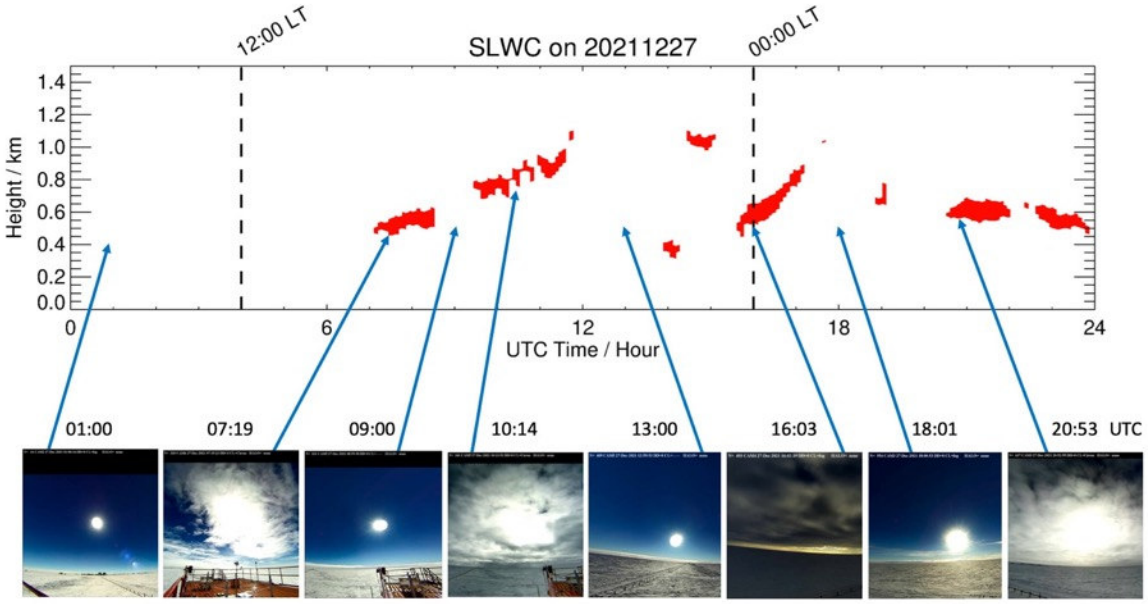

832

833 **Figure 2:** (Top) Time evolution (UTC, hour) of the SLWC (red areas) on 27 December 2021.
834 (Bottom, from left to right) Snapshots from the HALO-CAM video camera taken on: 01:00 (no
835 SLWC), 07:19 (SLWC), 09:00 (no SLWC), 10:14 (SLWC), 13:00 (no SLWC), 16:03 (SLWC),
836 18:01 (no SLWC) and 20:53 UTC (SLWC). The 00:00 and 12:00 local times (LT) are
837 highlighted by 2 vertical dashed lines.

838

839

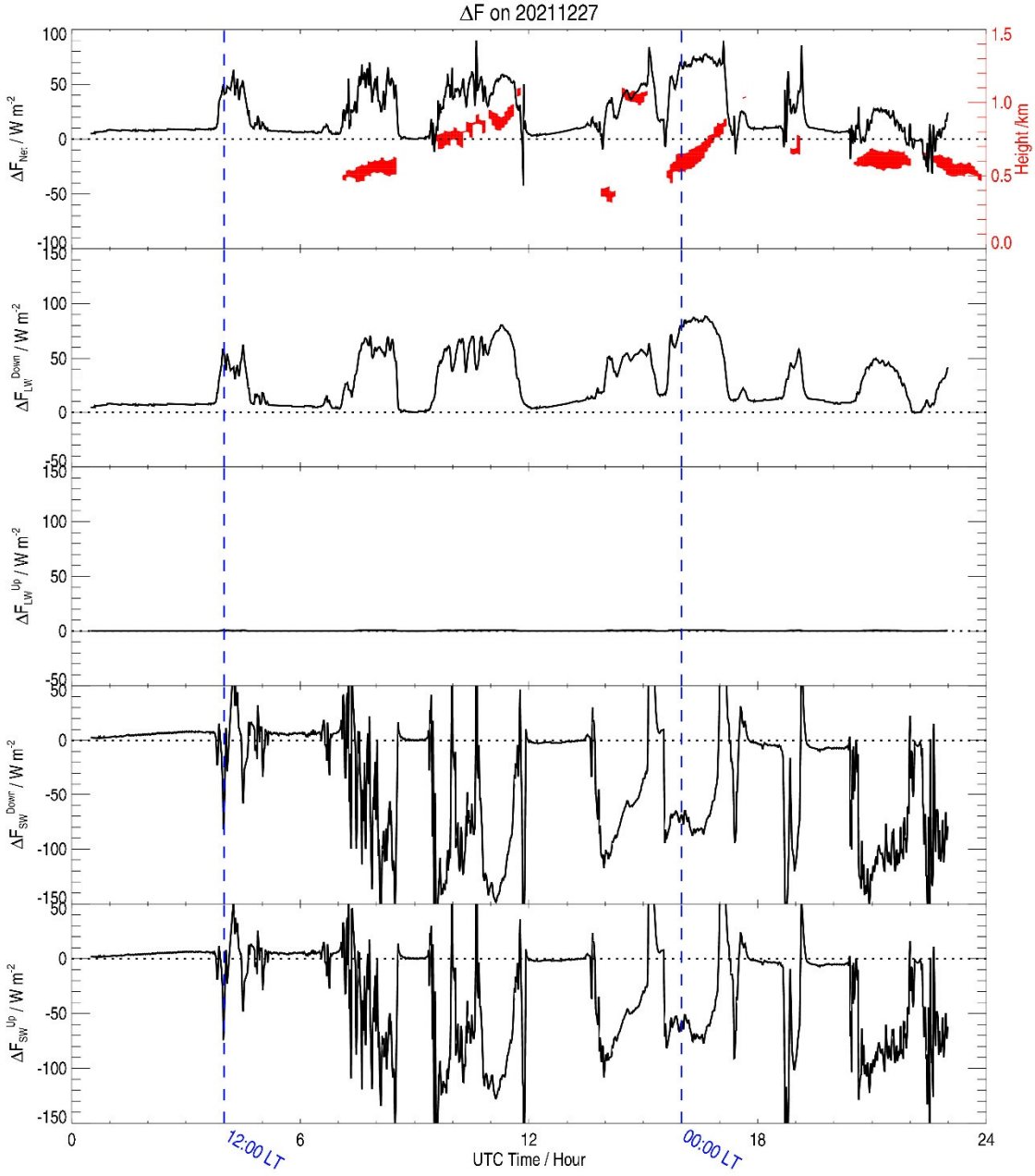

840

841 **Figure 3:** (from top to bottom) Time evolution (UTC, hour) of the cloud radiative forcing
842 (ΔF_{net}) (W m^{-2}) and its individual components: downward longwave (ΔF_{LW}^{Down}), upward
843 longwave (ΔF_{LW}^{Up}), downward shortwave (ΔF_{SW}^{Down}) and upward shortwave (ΔF_{SW}^{Up}) calculated
844 on 27 December 2021. The SLW cloud layer (if present) is highlighted by a red area in the
845 uppermost panel, with the height on the y-axis shown on the right. The 00:00 and 12:00 local
846 times (LT) are highlighted by 2 vertical blue dashed lines.

847

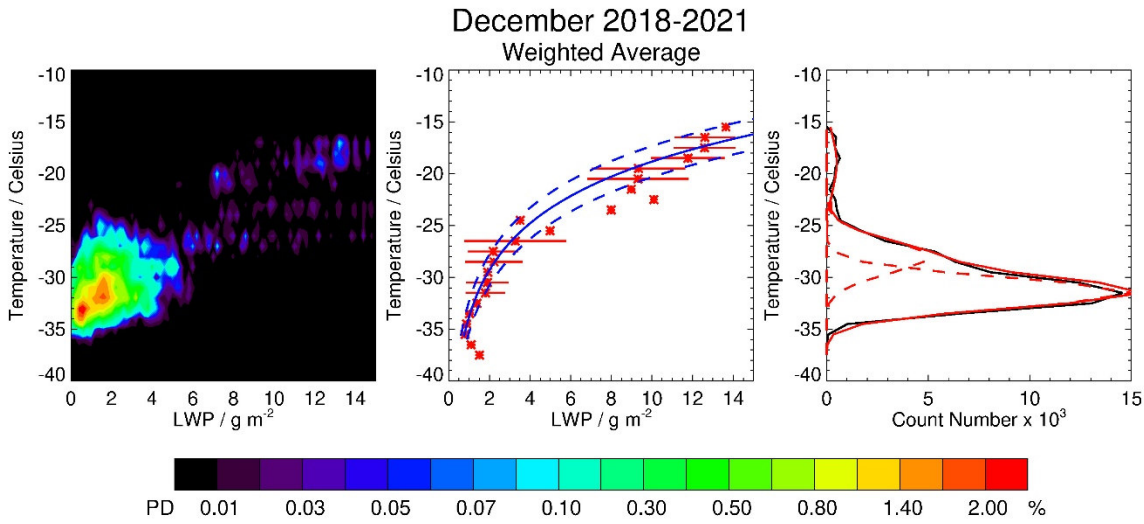

848

849 **Figure 4:** (Left) Probability Density (PD, %) of the temperature (°C) as a function of Liquid
850 Water Path (LWP, g m^{-2}) in the SLWCs in December 2018-2021. The Probability Density is
851 defined in the text. (Centre) Weighted-average LWP vs. temperature (red asterisks) with a fitted
852 logarithmic function (blue solid) encompassing the significant points (within the two dashed
853 blue lines). Horizontal bars represent 1-sigma variability in LWP per 1°C-wide bin. (Right)
854 Temperature as a function of count number per 1°C-wide bin (black solid line) fitted with three
855 Gaussian functions (red dashed curves). The sum of the three Gaussian functions is represented
856 by a red solid line.

857

858

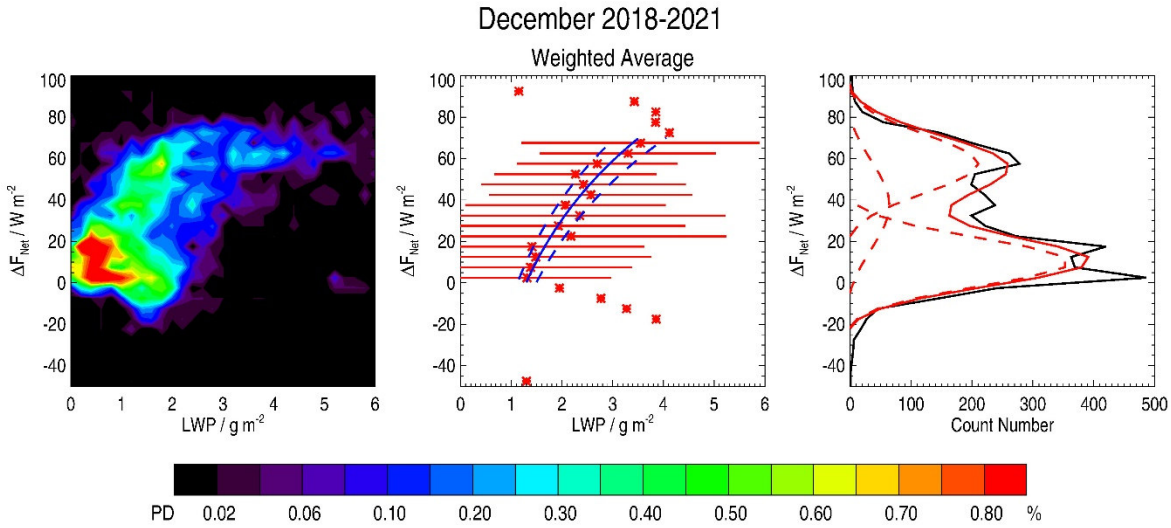

859

860 **Figure 5:** (Left) Probability Density (PD, %) of the cloud radiative forcing (ΔF_{net}, W m^{-2}) as a
861 function of Liquid Water Path (LWP, g m^{-2}) in the SLWCs in December 2018-2021. The
862 Probability Density is defined in the text. (Centre) Weighted-average LWP vs. ΔF_{net} with a
863 fitted logarithmic function (blue solid) encompassing the significant points (within the two
864 dashed blue lines). Horizontal bars represent 1-sigma variability in LWP per 5 W m^{-2}-wide bin.
865 (Right) ΔF_{net} as a function of count number per 5 W m^{-2}-wide bin (black solid line) fitted with
866 three Gaussian functions (red dashed curves). The sum of the three Gaussian functions is
867 represented by a red solid line.

868

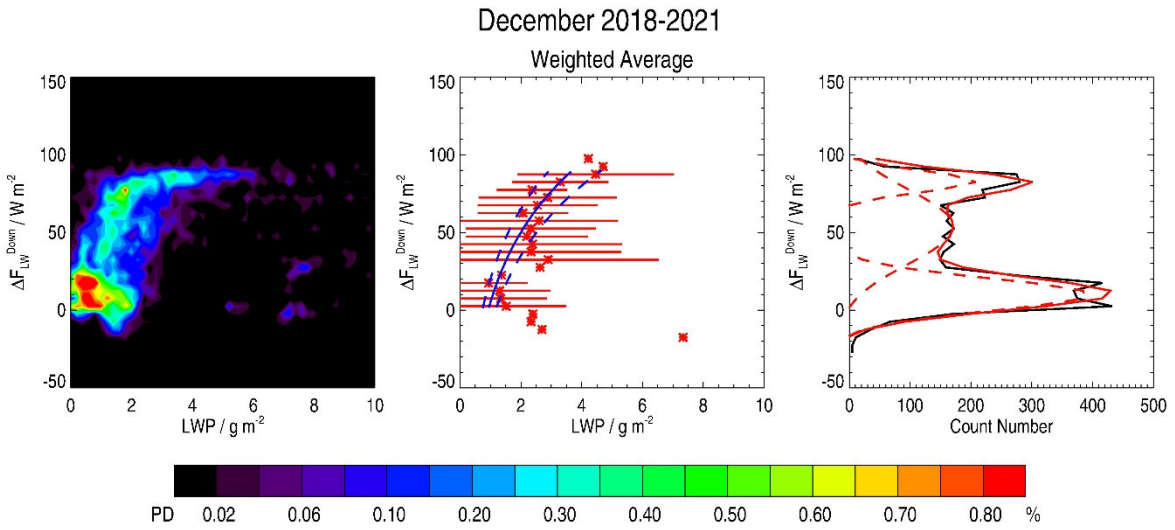

869

870 **Figure 6:** As in Figure 5 but for ΔF_{LW}^{Down}.

871

872

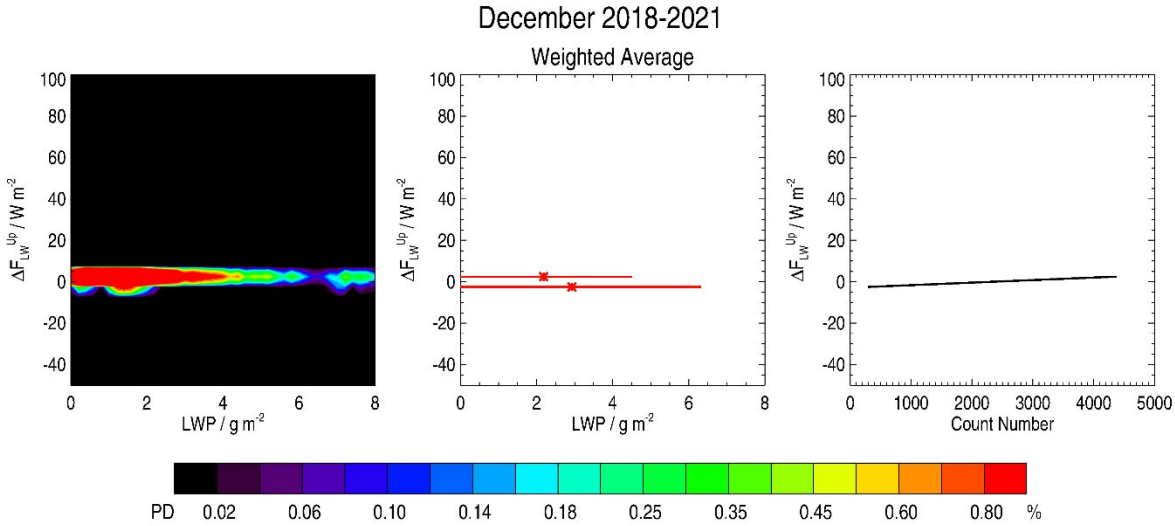

873

874 **Figure 7:** As in Figure 5 but for ΔF_{LW}^{Up}.

875

876

877

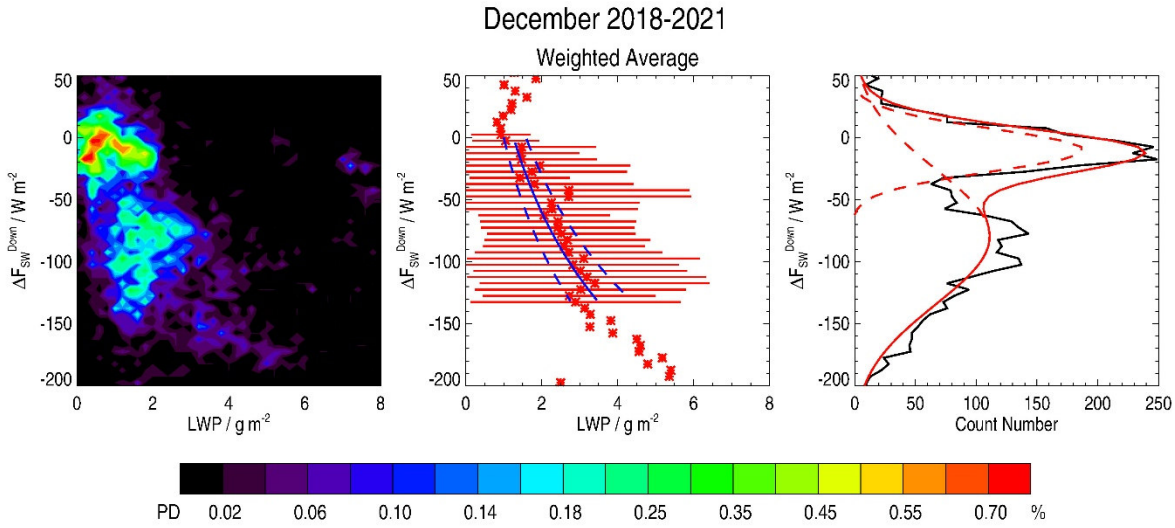

878

879 **Figure 8:** As in Figure 5 but for ΔF_{SW}^{Down}.

880

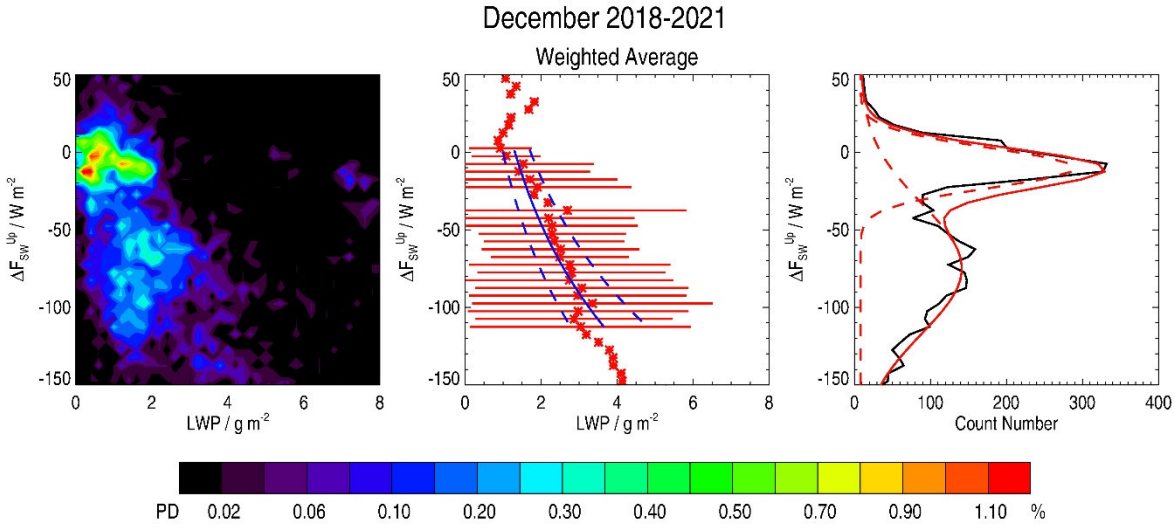

881

882 **Figure 9:** As in Figure 5 but for ΔF_{SW}^{Up}.

883

884

885

886

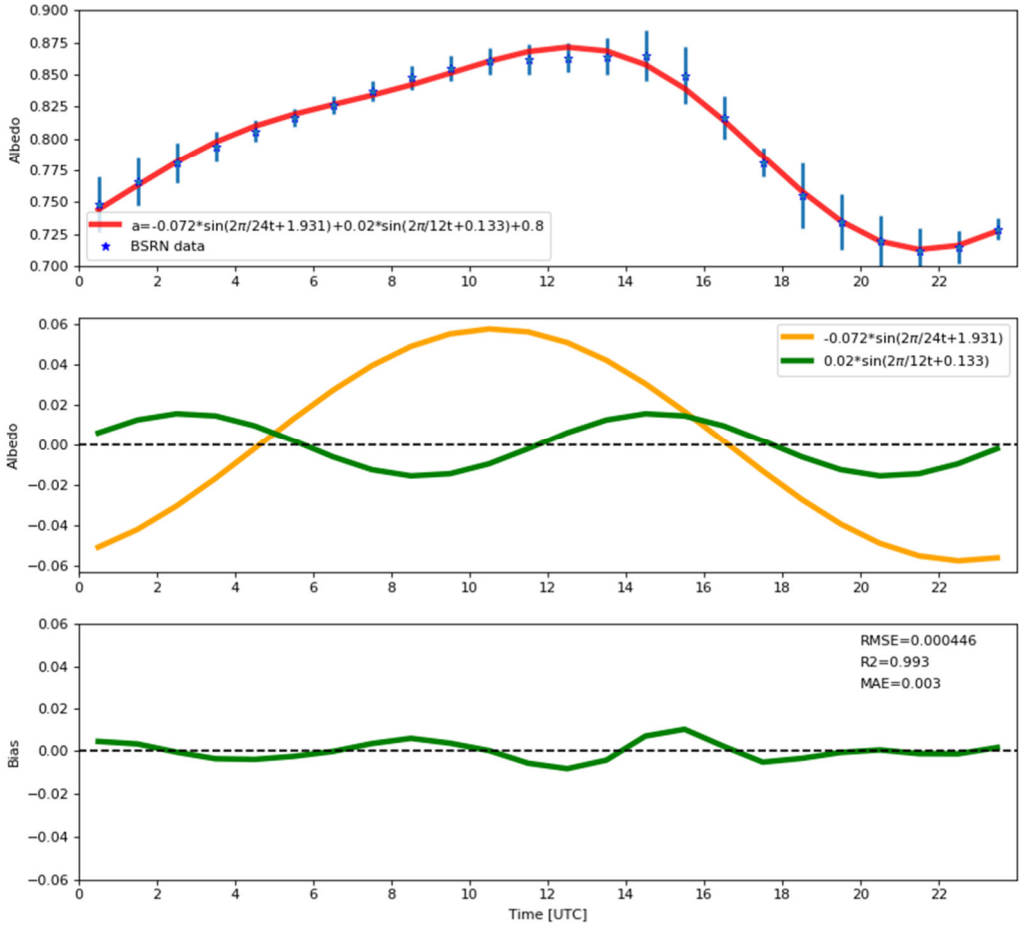

887

888 **Figure 10:** (Top) Hourly time evolution (UTC, hour) of the mean surface albedo observed by
889 the BSRN instruments and the associated standard deviation (blue star and vertical bar,
890 respectively) for the 5 cloud-free periods under consideration in our analysis together with the
891 fitted trigonometric function based on 2 sine functions (red line). (Centre) The 2 sine functions
892 fitting the hourly time evolution of the BSRN mean surface albedo. (Bottom) Hourly time
893 evolution (UTC, hour) of the albedo residuals (BSRN-fit, green line) and corresponding values
894 of associated Root Mean Square Error (RMSE), Coefficient of determination (R^2), and Mean
895 Absolute Error (MAE).

896

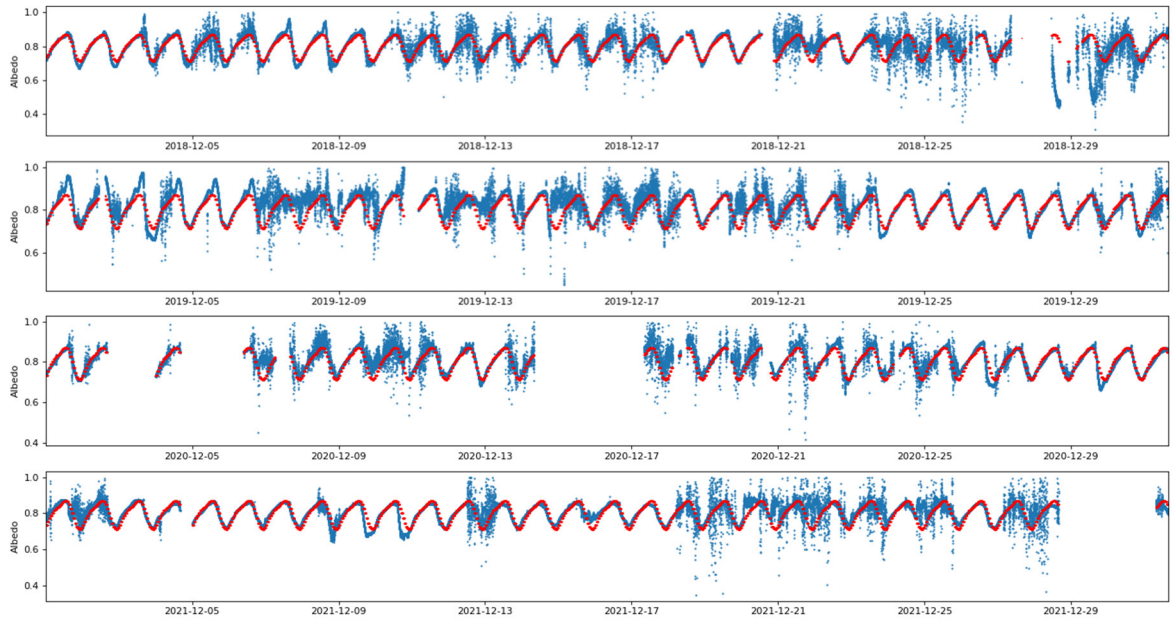

897

898 **Figure 11:** (from top to bottom) Hourly time evolution (UTC) of the surface albedo observed
899 by the BSRN instruments (blue), and using the fit based on 2 sine functions (red) for the whole
900 BSRN data set covering the month of December in: 2018, 2019, 2020 and 2021.

901